



## Research Article

# Calibration and Analysis of Mechanical Modeling for Traction Wire Rope of Mountainous Orchard Carrier

Yuping Ouyang,<sup>1,2,3</sup> Tianyu Wang ,<sup>1,2</sup> Tiansheng Hong ,<sup>3</sup> and Xudong Sun<sup>1</sup>

<sup>1</sup>School of Mechanical and Electrical and Vehicle Engineering, East China Jiaotong University, Nanchang 330013, China

<sup>2</sup>National and Local Joint Engineering Research Center for Fruit Intelligent Photoelectric Detection Technology and Equipment, Nanchang 330013, China

<sup>3</sup>School of College of Engineering, South China Agricultural University, Guangzhou 510642, China

Correspondence should be addressed to Tiansheng Hong; 2864445388@qq.com

Received 2 August 2021; Revised 12 September 2021; Accepted 27 September 2021; Published 25 October 2021

Academic Editor: Federico Guarracino

Copyright © 2021 Yuping Ouyang et al. This is an open access article distributed under the Creative Commons Attribution License, which permits unrestricted use, distribution, and reproduction in any medium, provided the original work is properly cited.

Low-cost transporting vehicles are a crucial routine for orchards in the mountainous place. As the core component of the mountainous orchard carrier, the wire rope is easily damaged due to frequent handling of agricultural materials. The mechanical model of carrier wire rope is the prerequisite for studying its damage mechanism. This paper first analyzes the load-bearing characteristics of the wire rope of the carrier and then uses the theory of differential geometry and the elasticity of the wire rope to establish the mechanical model of the wire rope side strand strain  $\varepsilon_0$  and the axial load  $T$  of the wire rope end face in the erect state and the radial contact pressure  $F_n$  of the wire rope at the bending section and the mechanical model of the axial tension  $F$  and the pulley diameter  $D$  of the wire rope end face. On the basis of the mechanical model and the wire rope geometric solid model, the finite element stress analysis of the wire rope in the vertical state was carried out to verify the accuracy of the wire rope stress model. The results show that when the wire rope was in the vertical state, the wire-wire contact stress was linear directly proportional to the load on the end face of the wire rope; the wire-wire contact stress between the strands was about 12 times that within the strand; the average error between the simulated value and calculated value was about 13.6%, proving the correctness of the established wire mechanics model. When the rope and wheel were in contact, the contact pressure of the outer wire of the side strand was only related to the axial tension of the wire rope end face and the diameter of the pulley but not to the elasticity modulus of the pulley.

## 1. Introduction

Traditional orchard planting with poor site conditions lacks scientific and reasonable planning, and fruit trees mostly grow in places with undeveloped transportation or even on steep terraced fields. A variety of track transport machines used in mountainous orchard have been developed at home and abroad, and the traction-based dual-track carrier is one of the representative models of this kind [1]. Wire rope traction-based carrier used in mountainous orchard is drawn by wire ropes, and the trolley travels along the track with a certain slope. The track is welded by 2 parallel tubes and auxiliary beams, and the slope of the track is set between 10° and 40° [2–5]. Figure 1 shows the application site of the

mountain track carrier. The driving device is placed on the mountain peak, the track is laid along the slope in multibend mountains, and the truck rides across the track. Power is transmitted through ropes between the truck and the driving device, so as to transport materials up and down the mountain. This carrier alleviates the labor intensity of fruit farmers in mountainous areas and effectively meets the delivery demand of transporting fruit and other agricultural resources in a labor-saving manner [6].

Steel wire rope is the core component of the carrier, and it is of great significance to study its failure behavior, and the mathematical modeling and mechanical modeling of the wire rope play an important role in the design and analysis. Since wire rope has been widely used, as for wire rope

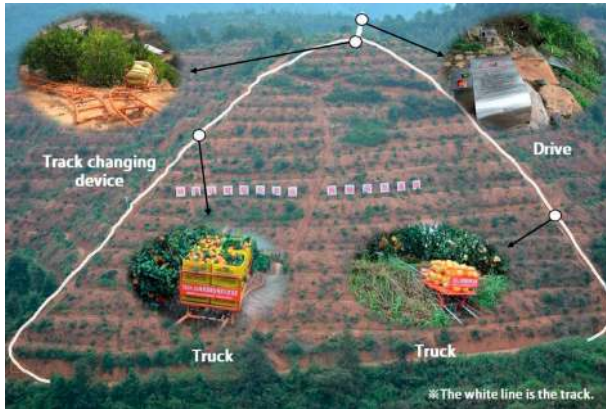


FIGURE 1: Application site of mountain track carrier.

modeling, many theoretical, analytical, and finite element models were developed to analyze their mechanical behaviors under various load conditions and predict their mechanical responses numerically [7]. Wire rope is a kind of spiral rope twisted by a certain number of strands, and the strands are made of multilayer wires with the rope core as the center. It has been applied in many fields such as industrial engineering, marine engineering, and civil engineering, as well as in drawbridge, crane, and elevator used during construction and mine hoist. As wire rope is characterized by advantages such as high strength, good softness, and high stability, it is mainly used for lifting, traction, straining, and load-bearing in material handling machinery, thus being widely used in machinery, robot, construction, mining, shipping, aerospace, and other fields [8, 9]. Wire ropes are in widespread use as structural members. A wire rope mostly consists of strands helically twisted around the central core. The strand is constituted of many wires helically wrapped around the inner wire. This implies that the rope geometry can be complicated [10]. Knapp [11] examined the effects of core/radius variation and presented a new stiffness matrix for straight cables subjected to tension and torsion, which can be applied not only to soft core of wire ropes but also to hard core structures. According to Costello [12–15] and Phillips and Costello [16] in consideration of the effect of Poisson's ratio premise, each wire will be considered as a spiral curved rod, with analysis of their mechanical structures. They generalized a nonlinear theory for bending and twisting of thin helical rods applied to a layer of wound helical wires without core. Velinsky [17, 18] extended the theory of Costello and Phillips by analyzing the mechanical response of multistrand structures. The modeling procedure was mainly based on nonlinear equations of equilibrium of a thin helical rod and analyzed torsion and bending stiffness of wire ropes. By studying eight different twist directions of the wire rope, Liu et al. argued that the twist directions mainly affected the torsion rather than the tension of the wire rope. Both the torsion and tension were closely related to the initial helical angle of the wire rope. This indicated that the overall mechanical properties of the wire rope could change with the twist direction and the helical angle of the wire rope [19]. Wu and Cao [20] used Frenet frame and differential

geometry to establish the mathematical model of the secondary spiral of wire rope. On this basis, the geometric parameters of the secondary spiral of wire rope were derived. As the equivalent mechanical model of the wire rope was established by using the Love theory of thin elastic rod, the calculation formulas of the equivalent elastic modulus and equivalent shear modulus of the wire rope were derived. Based on the geometric model of nonrotating wire rope, Pu et al. analyzed the causes of nonrotating wire rope's broken wire damage and established an identification model of nonrotating wire rope's broken wire damage, which was based on support vector machine (SVM). The results show that the model based on SVM was suitable for identifying the broken wire damage of nonrotating wire rope, thus providing a new effective tool for the identification of broken wire fault of nonrotating wire rope [21].

The orthotropic sheet model was first applied to cable modeling by Raoof and Kraincanic. This model is especially appropriate for multilayered strands and can be applied to theoretical analysis of large-diameter wire ropes [22]. Xue et al. [23] put forward two simplified cable calculation models based on the split-slip theory. With the suspension bridge of the Lijiang Railway in Yunnan as the background, they conducted fatigue test on the suspension cable with self-developed test devices. Wahid et al. [24] used steel strands, which were fractured in different percentages to constitute the outer strand of the wire rope, to characterize the mechanical behavior of the wire rope in service. Wang et al. [25] studied the stress and slip characteristics of elliptic and triangular strands. The variation range of maximum contact pressure of triangular steel strand was larger than that of the elliptic one. The maximum relative slip of triangular steel strand was much larger than that of the elliptic one, indicating that triangular steel strand was more prone to frictional fatigue damage.

According to the national standard GB/T5972-2009 "Cranes-Wire ropes-Care and maintenance, inspection and discard" and local engineering standard DG/T 211-2021 "Orchard Rail Transporter," Guangdong local standard DB44/T 1993-2017 "Dural Rail Transporting Machine for Mountainous Orchard," mountainous track carrier is different from traditional vertical hoist used in port, elevator used during construction, mine hoist, and aerial cable tramway, because its wire rope is affected by factors in traditional traction equipment such as long distance, high tension, multilayer winding and extrusion, and high corrosion, as well as new factors such as real-time variable tension, rotary torque, extrusion of restraining mechanism, and track vibration transformation. Studies have shown that the conveyor wire ropes are mainly subjected to loads such as axial tension, bending, and contact stress under normal service conditions [26]. The experimental and demonstration application results of orchard double-track conveyor show that the main forms of wire rope damage are wire breakage, wear, rust, and corrosion, among which wire breakage is the most obvious [27]. Meanwhile, wire ropes applied in different situations have different geometric model, mechanical model, stress, and strain, but for traction wire rope of mountainous track carrier, its mechanics

performance analysis is not yet clear. Therefore, this paper established a wire rope model to derive and predict its performance. In the previous work, this paper established the spatial geometric mathematical model of the carrier wire rope [28]. On this basis, taking the carrier wire rope in operation as the research object, using differential geometry and the theory of wire rope elasticity, a force model of the wire rope in the upright and bending state suitable for mountain orchard carriers is established. At the same time, the correctness of the mechanical model was verified by finite element analysis and experiments, thus providing theoretical basis for the optimization of the key components in mountainous carrier, the optimization of wire rope structure in complex mountainous environment, and the formulation of the criterion for rope replacement of corresponding equipment. The model also helps reduce expensive tests under different parameters and operating conditions.

## 2. Mechanics Modeling of the Carrier's Wire Rope in the Vertical State

**2.1. Simplified Route of Carrier Wire Rope Traction System.** The traction system of carrier used in mountainous orchard is a complex mechanical and electrical system. When the carrier is in operation, the motor, according to a certain speed curve, drives the rotating drum to rotate and wind the wire rope after passing the coupling, the electromagnetic brake, and the reduction gearbox. The driving force of the truck is provided by the driving drum, and the truck provides tension to the wire rope. The idler is used to avoid sliding friction between the wire rope and the rail beam and the ground; the constraint wheel ensures that the wire rope always runs along the track changing direction; the pulley is used for load-bearing and to change the moving direction of

wire rope. In the practical application of carrier, the track covers straight-line sections and bending sections, demonstrating that the carrier track is a space curve with many variations. When the carrier is in operation, the tension of the wire rope is always in a time-varying state due to the frequent handling of agricultural materials. When the wire rope is in the vertical state, the main damage is caused by "pull-pull fatigue"; in the bending state, the load of the wire rope is always changed by the way of "load in the straight-line section"–"load in the bending section"–"load in the straight-line section", which causes "bending fatigue" damage of the wire. For the convenience of analysis, this paper mainly considered horizontal and vertical turnings. As shown in Figure 2, a simplified schematic diagram of vertical/turning transport aircraft was established. There were one concave arc (A), two convex arcs (B/C), uphill, horizontal slopes, and downhill in the track.

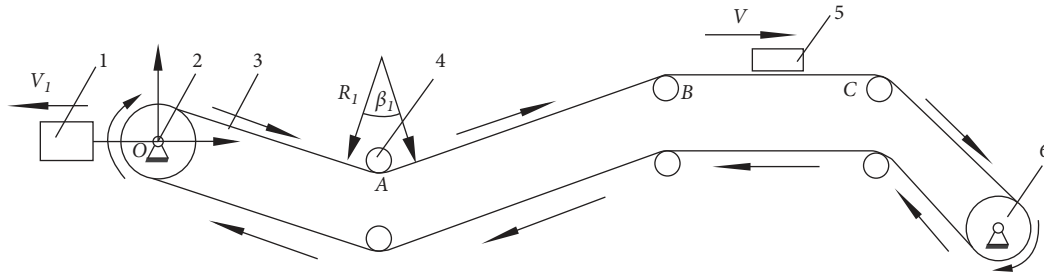
**2.2. Finite Element Model Construction of the Carrier's Wire Rope.** The spatial geometric characteristics of wire rope serve as the research basis of the mechanical model and failure behavior of wire rope and the key to explore the damage mechanism of the carrier's wire rope. Therefore, in order to know more intuitively the structure of traction wire rope of track carrier used in mountainous orchard, this section established wire rope 3D solid model. This was based on the spatial mathematical model expressions (i.e., equations (1) and (2)) [28] established by the researches mentioned before. MATLAB parameterization function, SolidWorks curve, scanning and solid array, and other functions were adopted to build such model.

In the equation of the  $k$  outer layer wire, the  $i$  strand of the straight-line section in wire rope is as follows:

$$OB_{ik}^x = \begin{bmatrix} r_0 \cos(\theta_i + \alpha_a) + r_2 [\cos \beta_0 \sin(\theta_i + \alpha_a) \sin(\theta_k - e_2 \alpha_a) - \cos(\theta_i + \alpha_a) \cos(\theta_k - e_2 \alpha_a)] \\ r_0 \sin(\theta_i + \alpha_a) + r_2 [-\cos \beta_0 \cos(\theta_i + \alpha_a) \sin(\theta_k - e_2 \alpha_a) - \sin(\theta_i + \alpha_a) \cos(\theta_k - e_2 \alpha_a)] \\ \frac{r_0 \alpha_a}{\tan \beta_0} + r_2 \sin \beta_0 \sin(\theta_k - e_2 \alpha_a) \end{bmatrix}. \quad (1)$$

In the equation of the  $k$  outer layer wire, the  $i$  strand of the bending section in wire rope is as follows:

$$O'B_{ik}^l = \left\{ \begin{array}{l} \sin(\theta_i + \alpha_a) [r_0 - r_1 \cos(\theta_k - e_2 \alpha_a)] - r_1 \cos \beta_0 \cos(\theta_i + \alpha_a) \sin(\theta_k - e_2 \alpha_a) \\ r_3 \cos e_3 \alpha_a - \cos e_3 \alpha_a \cos(\theta_i + \alpha_a) [r_0 + r_1 \cos(\theta_k - e_2 \alpha_a)] - r_1 \sin(\theta_k - e_2 \alpha_a) [\cos \beta_0 \cos e_3 \alpha_a \sin(\theta_i + \alpha_a) - \sin \beta_0 \sin e_3 \alpha_a] \\ r_3 \sin e_3 \alpha_a - \sin e_3 \alpha_a \cos(\theta_i + \alpha_a) [r_0 + r_1 \cos(\theta_k - e_2 \alpha_a)] - r_1 \sin(\theta_k - e_2 \alpha_a) [\cos \beta_0 \sin e_3 \alpha_a \sin(\theta_i + \alpha_a) + \sin \beta_0 \cos e_3 \alpha_a] \end{array} \right\}. \quad (2)$$



1. Wire rope tensioning device 2. Drive drum 3. Wire rope 4. Constraint wheel 5. Load pulley 6. Load trolley  
( $R_1$ . Turning radius  $\beta_1$ . Turning angle  $V$ . Running direction of load trolley  $V_1$ . Wire rope tensioning direction)

FIGURE 2: Simplified schematic diagram of a turn conveyor.

TABLE 1: Reference point coordinate of first share eighteenth wire.

Serial number of the reference point	X-axis coordinate	Y-axis coordinate	Z-axis coordinate
1	1.8017	0.4896	-0.0824
2	1.3254	3.0106	6.9692
3	-0.3422	3.3943	14.5669
4	-1.5710	1.2844	21.7153
5	-1.3648	-1.6788	28.3998
6	0.1395	-3.4792	35.6185
7	1.6916	-2.6984	43.2033
8	1.7732	-0.0522	50.1870
9	0.3201	2.4891	56.9145
10	-1.6804	3.1664	64.2900
11	-2.4863	1.4726	71.8032
12	-1.2831	-1.0666	78.6432
13	1.0580	-2.6482	85.4687
14	2.8853	-2.1368	92.9700

SolidWorks curve and scanning functions were used to establish the core wire of the side strand in wire rope, whose secondary spiral reference point coordinates then were obtained through MATLAB. These coordinates were made into TXT file, as shown in Table 1, which were the series coordinates of the reference point, the 18<sup>th</sup> wire (of the first strand). Then the SolidWorks "XYZ curve" function was adopted to import the prepared coordinate file in the parameter input settings. Finally, SolidWorks scanning, assembly, and solid array functions were used to build the 3D geometric model of the whole wire rope. Figures 3–5, respectively, show the 3D geometric models of single wire, wire-wire winding, the vertical section, and rope-wheel contact section [28].

**2.3. Solution of the Wire's Internal Stress.** Compared with the side strand wire, the force on the fiber core could be ignored, and the force on the whole rope was loaded into the side strand wire by default. Therefore, the stress characteristics of the side strand served as the key to analyzing the whole rope. The force on the side strand of the wire rope in the vertical state is shown in Figure 6. In order to deduce the force equation of each wire, in this paper, subscript 0 represented the side strand or its center wire, subscript 1 represented the inner wire of the side strand, and subscript 2 represented the outer wire of the side strand.

According to the mechanical equilibrium conditions and the relationship between the wire's bearing capacity and deformation, the following relational expressions could be obtained (Costello et al. [12–15, 29, 30]):

$$\left\{ \begin{array}{l} T = 6 \times (T_0 \cos \beta_0 + N_0^b \sin \beta_0), \\ T_0 = \frac{\pi}{4} E_0 D_0^2 \varepsilon_0, \\ N_0^b = H_0 k_0 - G_0^b \tau_0', \\ H_0 = \frac{\pi}{32} C_0 D_0^4 \Delta \tau_0, \\ G_0^b = \frac{\pi}{64} E_0 D_0^4 \Delta k_0. \end{array} \right. \quad (3)$$

In the formula,  $T$  is the axial load resultant force of whole rope (N).  $T_0$  is the tangential n-axis tension of side strand centerline (N).  $N_0^b$  is the normal shear force of side strand center line (N).  $H_0$  is the wire rope strand torque (N.m).  $G_0^b$  is the bending moment of the stock center line from the normal direction.  $E_0$  is the modulus of elasticity of side strand monofilament of steel wire rope (MPa).  $C_0$  is the shear modulus of wire rope side strand monofilament (MPa).  $k_0$  is the predeformation curvature of rope strand ( $\text{m}^{-1}$ ).  $\tau_0'$  is the deflection rate of rope strand after deformation.  $\Delta k_0$  is the curvature deformation before and after



FIGURE 3: Winding geometry entity between single wire and single wire.

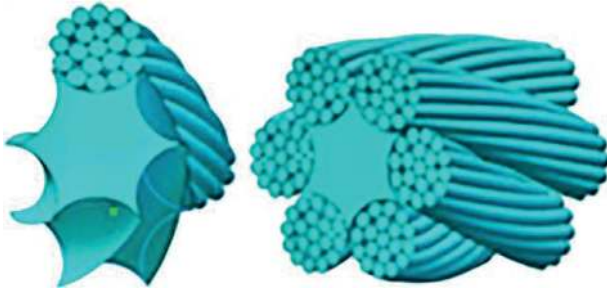


FIGURE 4: Three-dimensional entity model of upright wire rope.



FIGURE 5: Three-dimensional entity model of bending section wire rope.

deformation.  $\Delta\tau_0$  is the flexural deformation before and after deformation.  $\varepsilon_0$  is the strain of wire rope strand.  $D_0$  is the single-strand diameter (mm).

The spatial spiral equation, curvature, and torsion change rules of wire rope are the basis of studying the 3D solid modeling and mechanical model of the whole wire rope. Curvature is the extent to which a curve at a certain point bends, and torsion is the extent to which a space curve departs from being planar. There are definite curvature and

torsion at any point on the spatial spiral curve of the wire rope, and the curvature and torsion of the whole rope have certain change rules. The concept and properties of differential geometry are based on the Frenet coordinate system. The relationship between wire rope's curvature  $k$ , torsion  $\tau$ , and spatial spiral curve Eq.  $f(\alpha_a)$  is as follows (Costello and Knapp et al. [11–15, 31]):

$$k = \frac{\|f(\alpha_a)' \times f(\alpha_a)'\|}{\|f(\alpha_a)'\|^3} = \frac{\sqrt{(y'z'' - z'y'')^2 + (z'x'' - x'z'')^2 + (x'y'' - y'x'')^2}}{((x')^2 + (y')^2 + (z')^2)^{3/2}}, \quad (4)$$

$$\tau = \frac{(f(\alpha_a)', f(\alpha_a)'', f(\alpha_a)''')}{\|f(\alpha_a)' \times f(\alpha_a)''\|^2} = \frac{x'y''z''' + x''y'''z' + x'''y''z' - x'''y''z' - x'y'''z'' - x''y'z'''}{(y'z'' - z'y'')^2 + (z'x'' - x'z'')^2 + (x'y'' - y'x'')^2}. \quad (5)$$

Substituting known parameters into equations (4) and (5), the simplified expressions of curvature and torsion can be obtained:

$$k_0 = \frac{\|f_{OA}(\alpha_a)' \times f_{OA}(\alpha_a)''\|}{\|f_{OA}'(\alpha_a)\|^3} = \frac{\sin^2 \beta_0}{r_0}, \quad (6)$$

$$\tau_0 = \frac{(f_{OA}(\alpha_a)', f_{OA}(\alpha_a)'', f_{OA}(\alpha_a)''')}{\|f_{OA}'(\alpha_a) \times f_{OA}''(\alpha_a)\|^2} = \sin^2 \beta_0 \cos \beta_0. \quad (7)$$

After the deformation of the side strands of the wire rope, the helix radius  $r_0'$  of the strand is as shown in equation (8):

$$r_0' = r_0 - \mu \left[ \left( r_0 - \frac{D_0}{2} \right) \varepsilon + \frac{D_0}{2} \varepsilon_0 \right]. \quad (8)$$

From equations (6)–(8), the curvature  $k_0'$  and deflection  $\tau_0'$  of the steel wire after deformation can be obtained, as shown in equations (9) and (10). In the equation,  $\Delta\beta_0$  is the strand before and after the twist angle deformation in the whole rope the amount of deformation.

$$k_0' = \frac{2 \sin^2 (\beta_0 + \Delta\beta_0)}{2r_0 - \mu [(2r_0 - D_0)\varepsilon + D_0\varepsilon_0]}, \quad (9)$$

$$\tau_0' = \sin^2 (\beta_0 + \Delta\beta_0) \cos (\beta_0 + \Delta\beta_0). \quad (10)$$

According to equations (6), (7), (9), and (10), the curvature and deflection deformation of the steel wire can be

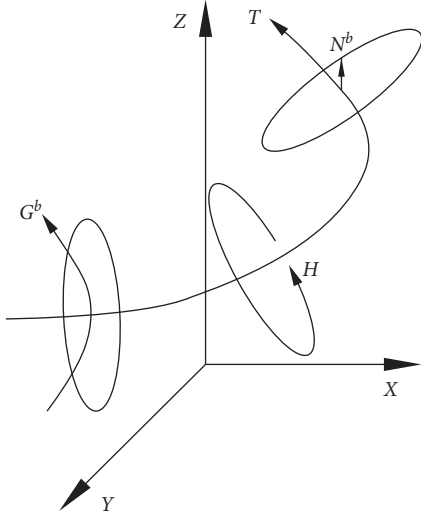


FIGURE 6: Force diagram of the side strand of wire rope in the vertical state.

obtained, as shown in equations (11) and (12), where  $\tau_0$  is the deflection rate of the strand before deformation.

$$\Delta k_0 = k_0 - k'_0 = \frac{\sin^2 \beta_0}{r_0} - \frac{2 \sin^2 (\beta_0 + \Delta \beta_0)}{2r_0 - \mu [(2r_0 - D_0)\varepsilon + D_0\varepsilon_0]}, \quad (11)$$

$$\Delta \tau_0 = \tau_0 - \tau'_0 = \sin^2 \beta_0 \cos \beta_0 - \sin^2 (\beta_0 + \Delta \beta_0) \cos (\beta_0 + \Delta \beta_0). \quad (12)$$

In Figure 7,  $P_0$  is the wire rope side strand lay length.  $S_s$  is the strand length in twist pitch.  $\alpha_s$  is the angle that the wire rope strands have turned (at this time the value is  $360^\circ$ ).

From the geometric relationship of the side strands of the wire rope after expansion in Figure 7, the strain  $\varepsilon$  of the whole rope can be obtained as

$$\varepsilon = \frac{(S_s + S_s \varepsilon_0) \cos (\beta_0 + \Delta \beta_0) - S_s \cos \beta_0}{S_s \cos \beta_0}. \quad (13)$$

Since  $\Delta \beta_0$  is extremely small, it can be considered that (Costello and Knapp et al. [11–15, 31])

$$\sin \Delta \beta_0 \approx \Delta \beta_0, \quad (14)$$

$$\cos \Delta \beta_0 \approx 1. \quad (15)$$

Bringing equations (14) and (15) into equation (13) gives

$$\Delta \beta_0 = \frac{\varepsilon - \varepsilon_0}{(1 + \varepsilon_0) \tan \beta_0}. \quad (16)$$

The process of calculating the relationship between the strain  $\varepsilon$  of the whole rope and the strain  $\varepsilon_0$  of the lateral strand is as “Appendix A”.

The wire rope of single-strand elastic modulus  $E_0$  and shear modulus  $C_0$  is as follows (the calculation process of single-strand elastic modulus  $E_0$  and shear modulus  $C_0$  is as “Appendix B”):

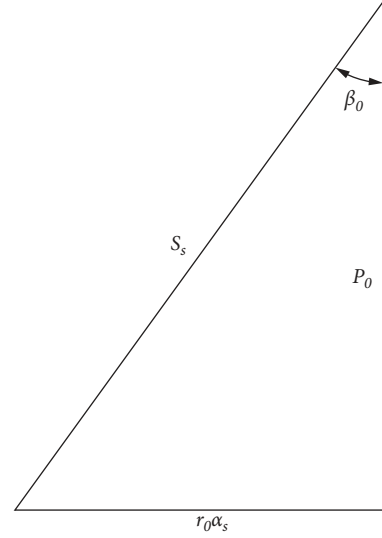


FIGURE 7: Expansion diagram of wire rope side femoral.

$$E_0 = e_8 E, \quad (17)$$

$$C_0 = \frac{19d^2}{D_0^2} C = e_7 C. \quad (18)$$

In summary, the functional relationship between the strand strain and the resultant force on the wire rope can be expressed as

$$\varepsilon_0 = f_\varepsilon (T). \quad (19)$$

According to equation (19), if the axial load of the end face of the wire rope was known, the relevant mechanical parameters of the rope strand and wire could be obtained. However, it would be too complex to simplify and express the process if the above derivation process was adopted to directly solve the relationship between the wire rope strain and the load in the vertical state. In this paper, MATLAB was used for calculation to establish the relational diagram between wire rope's strain and load, as shown in Figure 8. It could be seen from the diagram that the side strand strain of the wire rope was linear directly proportional to the axial load on the end face of the wire rope.

**2.4. Solution of Contact Stress between Upright Wires.** The contact between the steel wires of the upright steel wire rope includes two kinds of steel wire axes crossing each other and parallel, as shown in Figure 9,  $\varphi$  in Figure 9(a) represents the crossing angle between the steel wires, and the value is  $40^\circ$ . According to the Hertz contact theory, the contact area of the wire rope strands is elliptical. If the wire axes cross, the contact surfaces of the two wires are elliptical; if the wire axes are parallel, the contact surfaces of the two wires are rectangular.

The normal load  $X_{01}$  between the inner layer wires of the straight wire strands is related to the axial tensile force  $T_1$  of the inner layer wire and the twist angle  $\beta_1$ , and the normal load  $X_{12}$  between the outer layer wires is related to the axial tensile force  $T_2$  of the outer layer wire and the twist angle  $\beta_2$

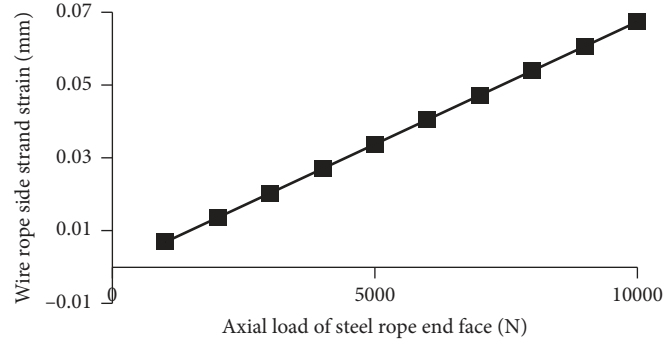


FIGURE 8: Relationship curve between wire rope end load and single-strand strain.

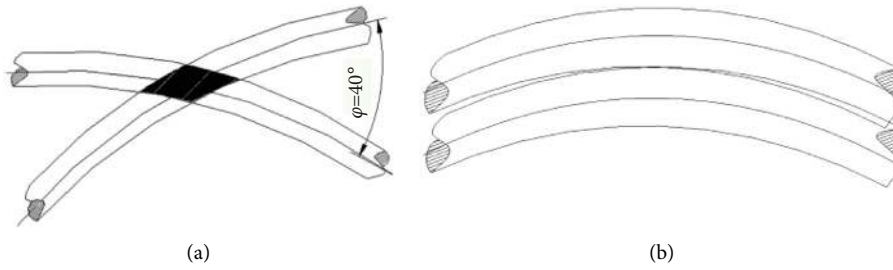


FIGURE 9: Contact diagram between wires and wires. (a) The wire axes of the strands cross each other (the angle  $\varphi = 40^\circ$  is the angle made by the tangents to the ropes middle line at the cross point). (b) The steel wire axes in the strands are parallel to each other.

[32], as shown in equations (20) and (21).  $T_1$  is not much different from  $T_2$ , and  $\beta_2$  is greater than  $\beta_1$ , so  $X_{12}$  is numerically greater than  $X_{01}$ . When calculating the maximum contact stress inside the wire rope, only  $X_{12}$  needs to be calculated.

$$X_{01} = 0.5T_1 \sin(2\beta_1), \quad (20)$$

$$X_{12} = 0.5T_2 \sin(2\beta_2). \quad (21)$$

The contact load  $X_{22}$  of the interstrand contact wire method is shown in equation (22), and the contact stress  $\sigma$  of the steel wire is calculated as shown in equation (23), where  $\gamma$  is the loose twist angle, and its value is equal to the strand twist angle  $\beta_0$ . Relevant, when  $\beta_0 \leq 6^\circ$ ,  $\gamma$  takes  $60^\circ$ ; when  $6^\circ < \beta_0 \leq 12^\circ$ ,  $\gamma$  takes  $50^\circ$ ; when  $\beta_0 > 12^\circ$ ,  $\gamma$  takes  $40^\circ$ .  $a$ ,  $b$  are the long axis and short axis length of the contact area between the steel wires, mm.

$$X_{22} = T_0 \sin \gamma, \quad (22)$$

$$\sigma = \frac{3X}{4\pi ab}. \quad (23)$$

When calculating the contact stress  $\sigma_{12}$  between the wires in the strand, take  $a = P_0$ ,  $b = d/8$ ,  $P_0$  is the twisting length of the wire in the strand, so

$$\sigma_{12} = \frac{6X_{12}}{\pi P_0 d}. \quad (24)$$

When calculating the wire contact stress  $\sigma_{22}$  between strands, take  $a = d/\sin\varphi$ ,  $b = d/3$ , so

$$\sigma_{22} = \frac{9X_{22} \sin \phi}{4\pi d^2}. \quad (25)$$

### 3. Mechanics Modeling of the Carrier's Wire Rope in the Bending State

**3.1. Bending Stress of Wire Rope in the Bending Section.** The bending section of orchard carrier's wire rope was reflected in the contact between the wire rope and the constraint wheel, pulley, and drum, as shown in Figure 10 [28]. The wear of the outer strand surface of the wire rope is caused by the friction between it and the pulley or the groove of the drum under the action of pressure. This wear was especially obvious at the place where the wire rope and the pulley touch when the suspension was accelerated or decelerated and reflected by the fact that external wire rope was ground into a plane shape. Insufficient or incorrect lubrication and the presence of dust and gravel could exacerbate the wear. When the rope and wheel were in contact, the bending stress and contact stress of the wire inside the rope changed greatly.

A certain wire of the rope was taken as the research object. According to the material mechanics, relevant expressions are as follows:



FIGURE 10: The wire rope is in contact with the restraining wheel, pulley, and drum.

$$\begin{aligned}
 X_{22} &= T_0 \sin \gamma, \\
 M^l &= \frac{EI}{r^l} = EIk^l, \\
 \Delta\sigma &= \frac{(M^l - M^x)d}{I} = E d(k^l - k^x), \quad (26) \\
 \sigma_l^l &= \sigma_l^x + \Delta\sigma_l, \\
 \sigma_X^l &= T_1^l + \sigma_l^l.
 \end{aligned}$$

In the formula,  $r^x$  is the curvature radius of vertical steel wire (mm).  $I$  is the inertia moment of steel wire section to neutral axis (mm).  $r^l$  is the radius of curvature of the wire rope bending section (mm).  $M^x$  is the wire bending moment of the vertical section of the wire rope (N.m).  $M^l$  is the wire bending moment of wire rope bending section (N.m).  $k^x$  is the steel wire curvature of the upright section of the wire rope ( $\text{mm}^{-1}$ ).  $k^l$  is the steel wire curvature of the bending section of the wire rope ( $\text{mm}^{-1}$ ).  $E$  is the elastic modulus of steel wire (MPa).  $d$  is the diameter of steel wire (mm).  $\Delta\sigma$  is the moment the wire rope enters the bending section from the straight section, the maximum bending stress increase of any steel wire in the rope.  $\sigma_l^x$  is the bending stress of steel wire in the vertical section of steel wire rope (MPa).  $\sigma_l^l$  is the maximum bending stress of steel wire in bending section of wire rope (MPa).  $\Delta\sigma_l$  is the bending stress increment.  $\sigma_X^l$  is the maximum normal stress of wire rope side wire in bending section (MPa).  $T_1^l$  is the axial tensile stress of steel wire in inner layer of bending section of steel wire rope (MPa).  $T_2^l$  is the axial tensile stress of the steel wire in the outer layer of the bending section of the wire rope (MPa).

### 3.2. Contact Stress of Wire Rope in the Bending Section.

When the rope is being coiled onto the wheel, if the contact between the wire rope and the side wall of the rope groove is not considered, the wear between the rope and the pulley is mainly caused by the contact stress between the two. The contact between the rope and wheel is actually the contact between the outer wire and the pulley groove's surface, but it is converted to dense point contact by the spiral structure of the wire rope. The schematic diagram of the contact between the wire rope and the pulley is shown in Figure 11.

It is assumed that the total length of the rope-wheel contact is  $L$ ; the twist length of the side strand in the rope is  $S$ ;

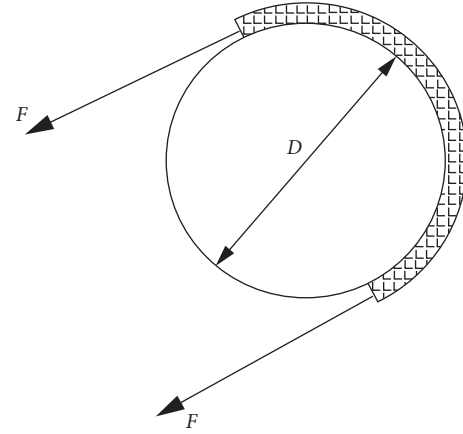


FIGURE 11: Contact diagram between wire rope and pulley.

and the twist length of the outer wire in the side strand is  $P_n$ ; the wire rope is composed of  $N_w$  outer strands, and each share has  $N_c$  side wires; the twist angle of the side strand in the rope is  $\beta_0$ ; the depth of the wire rope embedded in the groove of the pulley wheel is half of the outer diameter of the wire rope. According to the above-given data, the actual number of rope-wheel contact points could be calculated as  $N_m$ :

$$N_m = \frac{SN_c}{2 \sin \beta_0 P_n} \frac{LN_w}{S} = \frac{LN_c N_w}{2 \sin \beta_0 P_n}. \quad (27)$$

According to the geometric relationship in Figure 11, the length of the rope-wheel contact section is shown in equation (28), where  $\theta$  is the contact angle between the rope and wheel;  $d$  and  $D$  are the diameters of the wire rope and the pulley, respectively.

$$L = \frac{(D + d)\theta}{2}. \quad (28)$$

As equation (28) was substituted into equation (27), it could be obtained that the number of contact points between the wire rope and the wheel groove is

$$N_m = \frac{(D + d)\theta N_c N_w}{4 \sin \beta_0 P_n}. \quad (29)$$

The rope-wheel contact stress was evenly distributed. Microsegment of the wire rope with a central angle of  $\Delta\theta$  was selected for stress analysis, as shown in Figure 12.



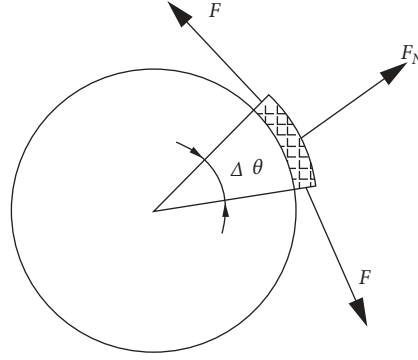


FIGURE 12: Microsection wire rope contacting force diagram between pulley and wire rope.

When the carrier was in operation, a certain microsegment of wire rope was in instantaneous contact with the wheel groove. It could be approximately considered that the axial tension  $F$  at any position within the wire rope where the rope and wheel contact was all the same. The tension was tangent to the central axis of the wire rope, and the contact pressure  $F_N$  between the wire rope and the pulley groove always followed the normal direction of the pulley groove's arc surface. According to the force balance of the wire rope in the microsegment, the contact pressure between the wire rope and the pulley groove is as follows:

$$F_N = 2F \sin\left(\frac{\Delta\theta}{2}\right). \quad (30)$$

According to equation (30), when  $\Delta\theta$  was extremely small, it could be considered that  $\sin(\Delta\theta/2) = \Delta\theta/2$ , so the sum of  $F_N$ 's values in the range of  $\theta$  (contact wrap angle between the wire rope and the pulley) could be expressed as follows:

$$\sum_{i=1}^N F_N = \sum_{i=1}^N 2F \sin\left(\frac{\Delta\theta_i}{2}\right) = \sum_{i=1}^N F \Delta\theta_i = \int_0^\theta F d\theta = F\theta. \quad (31)$$

In conclusion, the radial average pressure  $F_a$  (borne by each contact point between the wire rope and the pulley groove) is shown in equation (32). In the equation,  $r_0$  is the spiral radius (twisting radius) of the strand in the rope and  $\alpha_a$  refers to the angle the strand in the rope covers when the rope is twisted.

$$F_a = \frac{\sum_{i=1}^N F_N}{N_m} = \frac{4F \sin \beta_0 P_n}{(D+d)N_w N_c} = \frac{4FP_n r_0 \alpha_a}{(D+d)N_w N_c \sqrt{r_s^2 + r_0^2 \alpha_a^2}}. \quad (32)$$

According to equation (32), when the type and diameter of the wire rope were determined, the contact pressure of the side strand wire where the rope and wheel contact was only related to the axial tension of the wire rope's end face  $F$  and the pulley's diameter  $D$ . The pressure was also directly proportional to the axial tension of the wire rope, was inversely proportional to the pulley diameter, and had nothing to do with the pulley's elastic modulus. To reduce the rolling friction force between the pulley and the wire rope, the

material with small friction coefficient and large strength should be used to make the pulley.

#### 4. Finite Element Model Construction and Force Analysis of Wire Rope

**4.1. Finite Element Model Construction of the Conveyor's Wire Rope.** 3D solid model of wire rope was imported into ANSYS Workbench. In the previous research [28], we established the space spiral equation of the carrier wire rope in the upright and bent state and obtained the obvious periodic change law of the curvature and deflection of the straight and curved sections of this kind of wire rope through the mathematical model. As the symmetric characteristics of the wire rope structure were considered, 1/6-twist-length wire rope was selected as the research object to shorten the simulation time, as shown in Figure 13. The elastic modulus  $E$  was tested to be 74 GPa, and the tensile test site is shown in Figure 14; the test data are shown in Table 2; Poisson's ratio was 0.3 [15, 16]. Mesh division was conducted on the wire rope by "mesh" command, and solid45 unit was selected to discrete the structure. The finite element model of the wire rope after mesh division is shown in Figure 15. The total unit number of finite element mesh is 613,858, and the total number of nodes is 2,941,946. Each node contains 3 degrees of freedom.

**4.2. Finite Element Force Analysis of Wire Rope in the Vertical Section.** The results of the steel wire failure test show that the axial force damage is the largest [27]. An end face of the wire rope was selected as the target face, to which displacement constraints in  $X$ ,  $Y$ , and  $Z$  directions were applied. Then axial tensile load was applied to the other end face of the wire rope. Finally, the solution was made. The stress results for each node could be referred to in the ANSYS Workbench postprocessor. When the tensile load on the end face was 8000 N, the stress cloud map of each wire in the rope is shown in Figure 16. Similarly, the stress cloud map of the wire inside the rope could also be analyzed when the axial tension of the end face was ranging from 1000 N to 7000 N. As the simulated values and calculated values of the maximum wire contact force reflected in the stress cloud diagram above were summarized, their comparison results when the wire rope was under different

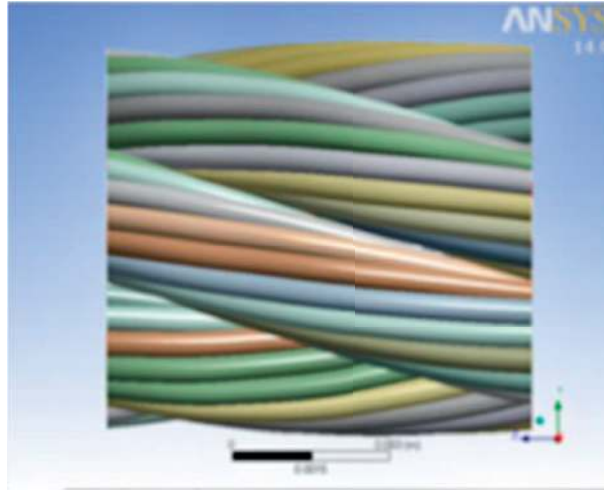


FIGURE 13: Three-dimensional model of wire rope.



FIGURE 14: Wire elastic modulus test scene. 1. Wire clamp 2. Steel wire 3. Precision electronic universal material testing machine 4. Computer.

TABLE 2: Material tensile test data of wire rope.

Tensile stress (MPa)	Plastic strain (mm)
1121.02	2.0
1121.02	1.6
1121.02	1.5
1579.62	2.1
1426.75	1.7
815.29	1.3
1273.89	1.4
1070.06	1.2
866.24	1.0
866.24	1.7

coaxial tension could be obtained, as shown in Table 3. Data in Table 3 were made into a curve diagram, as shown in Figure 17.

It could be seen from the stress cloud diagram of wire-wire contact shown in Figure 16 and Table 3 that the maximum contact stress occurred in the contact wire between strands when the wire rope was in the vertical state. As the wire-wire contact stress within the strand was compared with that between strands, it was found that the latter was much greater than that of the former. The contact stress between strands was about 12 times that within the strand. It could be seen from Figure 17 that the contact stress between the wire rope in the vertical state was linear, directly

proportional to the load on the end face of the wire rope. The average error between the simulated value and the calculated value was about 13.6%, proving that the established equation of the wire rope's stress was correct.

In Table 3, as the contact stress equation only calculated the contact stress between wires without considering the bending stress, etc., the calculated value was relatively small compared with the simulated value. There was a big difference between the calculated value and the simulated value of the wire-wire contact stress between strands. The reason was that the equation of the contact stress between the wires only took into account the axial tension of the wire when the wire was wound into strands, without taking into account the influence of factors, such as the shear stress between the wires. In conclusion, when the wire rope in the vertical state had borne axial tension, the contact area between the strands of the wire rope should be the focus of study, because the area was very likely to suffer fretting wear between the wires.

## 5. Discussion

In the previous work, we established the spatial geometric mathematical model of the carrier wire rope. On this basis, taking the carrier wire rope in operation as the research object, using differential geometry and the theory of wire rope

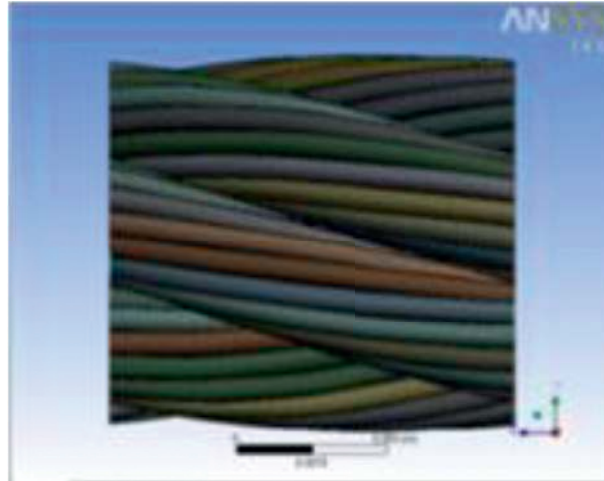


FIGURE 15: ANSYS Workbench mesh map.

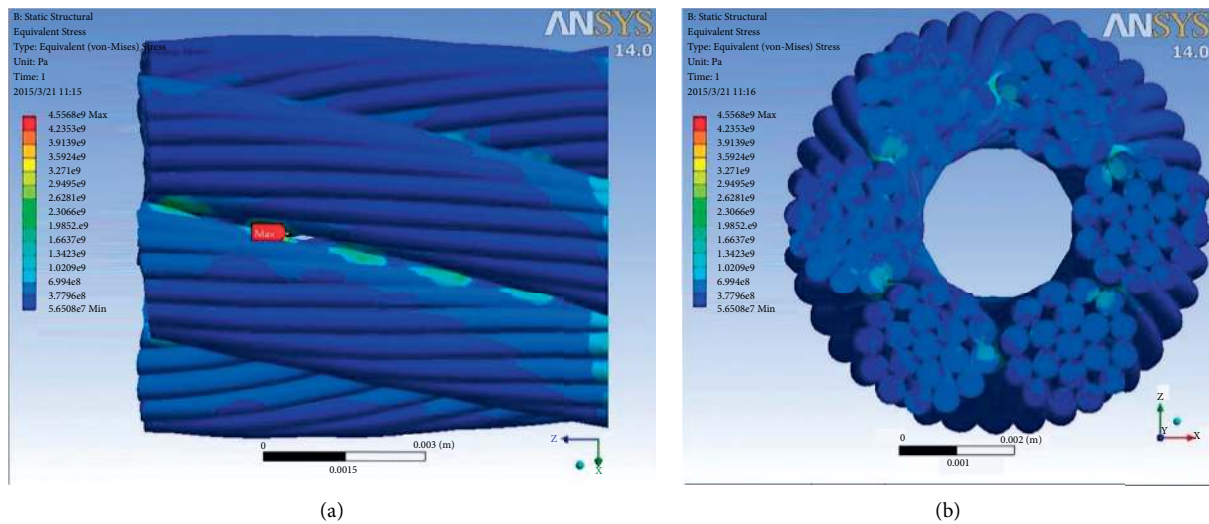


FIGURE 16: Wire rope simulation result at axial tension 8000 N under ANSYS Workbench.

TABLE 3: Maximum contact stress simulation and calculation results by different wire rope end load.

Axial load of the wire rope (N)	Wire-wire contact stress within the strand (MPa)		Wire-wire contact stress between strands (MPa)	
	Calculated value	Simulated value	Calculated value	Simulated value
1000	0.2918	47.197	492.3	569.6
2000	0.5835	94.394	984.5	1139.2
3000	0.8753	141.591	1476.8	1708.8
4000	1.1671	188.788	1969.1	2278.4
5000	1.4588	235.985	2462.2	2848
6000	1.7506	283.182	2953.6	3417.6
7000	2.0424	330.379	3445.9	3987.2
8000	2.3342	377.576	3938.1	4556.8

elasticity, a force model of the wire rope in the upright and bending state suitable for mountain orchard carriers is established.

However, this article also has obvious shortcomings. This article does not verify the response of the wire rope under the bending state. The response of a wire rope in a

bending state in a real environment is a dynamic nonlinear problem. Due to the limited experimental conditions, we cannot verify the response of the wire rope in the bending state through experiments. This article only verifies whether the simulation model in the bending state is reliable. This shortcoming also provides a research direction

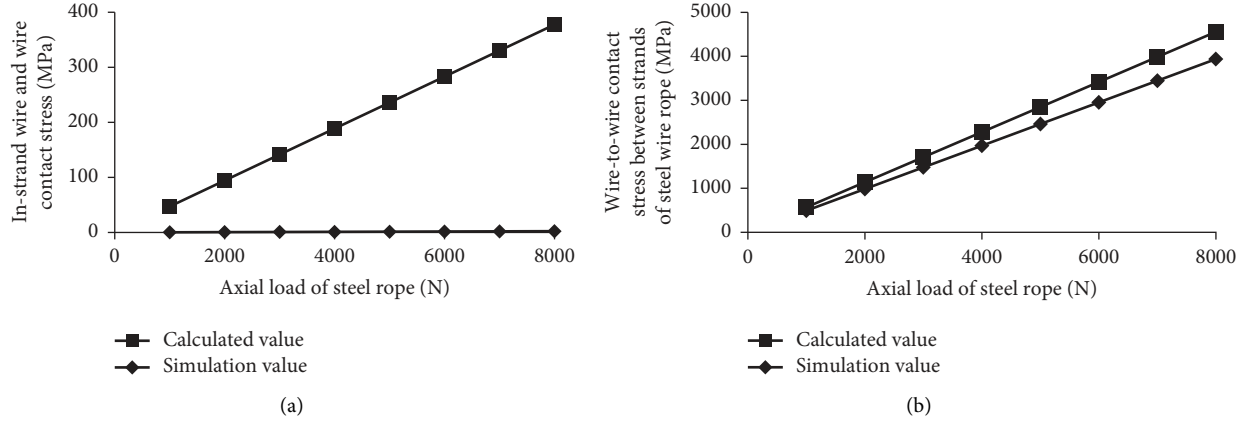


FIGURE 17: Maximum contact stress relationship curve by different wire rope end load. (a) In-strand wire and wire contact stress. (b) Wire-to-wire contact stress between strands of steel wire rope.

for our future work. The test demonstration application effect of the orchard double-track conveyor shows that broken wires, abrasion, rust, and corrosion are the main manifestations of wire rope damage, and the broken wires are the most obvious. On the other hand, considering that the operating environment of the steel wire rope of the carrier is complicated, the most contact with it during operation is the grease. For this reason, in the next work, we will analyze the external factors that affect the damage of the wire rope: the influence of grease stain on the damage of the wire rope. Including the formation mechanism of grease stain and the characteristics of grease stain abrasives, it is concluded that the grease stain causes fatigue, wear, and corrosion of the steel wire rope and other comprehensive damage problems. It provides a theoretical basis for the optimization of the key components of the mountain carrier, the optimization of the steel wire rope structure in the complex environment of the mountain, and the establishment of the rope replacement guidelines for the corresponding equipment.

## 6. Conclusions

- (1) This article describes the predictive trend model. Under normal operating conditions of the carrier, the model can predict the stress characteristics of the wire rope. After the load-bearing characteristics of the carrier's wire rope were analyzed, the stress models of  $6 \times 19 + FC$  wire rope in both the vertical and bending states were established. Based on the built mechanical model, MATLAB was used to calculate and analyze the wire-wire contact stress between the strands and within the strand, as well as the contact stress between the outer wire of the side strand and the pulley.
- (2) Solid model of the wire rope was imported into ANSYS Workbench for finite element force analysis. The results show that when the wire rope was in the vertical state, the wire-wire contact stress was in linear proportion to the load on the end face of the wire rope; the wire-wire contact stress between the

strands was much larger than and was 12 times that within the strand; the average error between the simulated value and the calculated value was about 13.6%, proving that the established wire mechanical model was correct.

- (3) When the rope and wheel were in contact, the bending stress and contact stress of the wire inside the rope changed greatly. It can be known from the established mechanical model that the contact pressure of the outer wire of the side strand was only related to the axial tension of the wire rope end face and the diameter of the pulley. This contact stress was directly proportional to the axial tension of the wire rope end face and inversely proportional to the diameter of the pulley but had nothing to do with the elasticity modulus of the pulley. To reduce the rolling friction force between the pulley and the wire rope, the material with a small friction coefficient and large strength should be used to make the pulley.

## Appendix

### A. The Relationship between the Strain $\varepsilon$ of the Whole Rope and the Strain $\varepsilon_0$ of the Lateral Strand

The process of calculating the relationship between the strain  $\varepsilon$  of the whole rope and the strain  $\varepsilon_0$  of the lateral strand is as follows:

According to the Pythagorean theorem in Figure 7:

$$S_s(P_0, \alpha_s, r_0) = \sqrt{P_0^2 + r_0^2 \alpha_s^2}. \quad (\text{A.1})$$

Differentiating the function of equation appendix A.1 gives

$$\Delta S_s = \frac{P_0 \Delta P_0}{\sqrt{P_0^2 + r_0^2 \alpha_s^2}} + \frac{r_0 \alpha_s^2 \Delta r_0}{\sqrt{P_0^2 + r_0^2 \alpha_s^2}} + \frac{r_0^2 \alpha_s \Delta \alpha_s}{\sqrt{P_0^2 + r_0^2 \alpha_s^2}}. \quad (\text{A.2})$$

For the two ends of equation appendix A.2, the division of  $S_s$  can obtain the strain  $\varepsilon_0$  as

$$\varepsilon_0 = \frac{P_0^2 \varepsilon}{S_s^2} + \frac{r_0 \alpha_s^2 \mu [(2r_0 - D_0)\varepsilon - D_0 \varepsilon_0]}{2S_s^2} + \frac{r_0^2 \alpha_s \Delta \alpha_s}{S_s^2}. \quad (\text{A.3})$$

Ignoring the torque during the stress of the wire rope, that is,  $\Delta \alpha_s = 0$ , the relationship between  $\varepsilon$  and  $\varepsilon_0$  can be obtained as

$$\varepsilon = \frac{2r_0 + \mu D_0 \sin^2 \beta_0}{2r_0 \cos^2 \beta_0 + \mu (2r_0 - D_0) \sin^2 \beta_0} \varepsilon_0. \quad (\text{A.4})$$

Let  
 $e_4 = ((2r_0 + \mu D_0 \sin^2 \beta_0) / (2r_0 \cos^2 \beta_0 + \mu (2r_0 - D_0) \sin^2 \beta_0))$   
 get  
 $\varepsilon = e_4 \varepsilon_0.$  (A.5)

## B. The Relationship between the Elastic Modulus of Single Strand $E_0$ and the Elastic Modulus of Monofilament $E$

In a single strand, according to the relationship between wire force and deformation:

$$T_0 = \frac{\pi}{4} Ed^2 \varepsilon_0 + 6 \times (T_1 \cos \beta_1 + N_1^b \sin \beta_1) + 12 \times (T_2 \cos \beta_2 + N_2^b \sin \beta_2), \quad (\text{B.1})$$

$$\left\{ \begin{array}{l} T_1 = \frac{\pi}{4} Ed^2 \varepsilon_1 \\ N_1^b = H_1 k_1 - G_1^b \tau_1' \\ H_1 = \frac{\pi}{32} Cd^4 \Delta \tau_1 \\ G_1^b = \frac{\pi}{64} Ed^4 \Delta k_1 \end{array} \right\} \left\{ \begin{array}{l} T_2 = \frac{\pi}{4} Ed^2 \varepsilon_2 \\ N_2^b = H_2 k_2 - G_2^b \tau_2' \\ H_2 = \frac{\pi}{32} Cd^4 \Delta \tau_2 \\ G_2^b = \frac{\pi}{64} Ed^4 \Delta k_2 \end{array} \right. \quad (\text{B.2})$$

In the same way as formulas (6)–(16) and Appendix A, the expressions of related mechanical parameters of inner layer filament and outer layer filament can be derived:

$$\left\{ \begin{array}{l} \varepsilon_1 = e_5 \varepsilon_0 = \frac{2r_1 \cos^2 \beta_1 + \mu (2r_1 - d) \sin^2 \beta_1}{2r_1 + \mu d \sin^2 \beta_1} \varepsilon_0 \\ \Delta \beta_1 = \frac{1 - e_5}{(1 + e_5 \varepsilon_0) \tan \beta_1} \varepsilon_0 \\ \Delta k_1 = k_1 - k_1' = \frac{\sin^2 \beta_1}{r_1} - \frac{2 \sin^2 (\beta_1 + \Delta \beta_1)}{2r_1 - \mu (2r_1 - d + e_5 d) \varepsilon_0} \\ \Delta \tau_1 = \tau_1 - \tau_1' = \sin^2 \beta_1 \cos \beta_1 - \sin^2 (\beta_1 + \Delta \beta_1) \cos (\beta_1 + \Delta \beta_1) \end{array} \right. , \quad (\text{B.3})$$

$$\left\{ \begin{array}{l} \varepsilon_2 = e_6 \varepsilon_0 = \frac{2r_2 \cos^2 \beta_2 + \mu (2r_2 - d) \sin^2 \beta_2}{2r_2 + \mu d \sin^2 \beta_2} \varepsilon_0 \\ \Delta \beta_2 = \frac{1 - e_6}{(1 + e_6 \varepsilon_0) \tan \beta_2} \varepsilon_0 \\ \Delta k_2 = k_2 - k_2' = \frac{\sin^2 \beta_2}{r_2} - \frac{\sin^2 (\beta_2 + \Delta \beta_2)}{r_2 - \mu (r_2 - (d/2) + (d/2) e_6) \varepsilon_0} \\ \Delta \tau_2 = \tau_2 - \tau_2' = \sin^2 \beta_2 \cos \beta_2 - \sin^2 (\beta_2 + \Delta \beta_2) \cos (\beta_2 + \Delta \beta_2) \end{array} \right. .$$

The relationship between the single-strand elastic modulus  $C_0$  and the monofilament elastic modulus  $C$  is shown in equation appendix B.4, where  $e_7$  is a constant.

$$C_0 = \frac{19d^2}{D_0^2}C = e_7C. \quad (\text{B.4})$$

$$\frac{\pi}{4}E_0D_0^2\varepsilon_0 = T_0 = \frac{\pi}{4}Ed^2\varepsilon_0 + 6 \times (T_1 \cos \beta_1 + N_1^b \sin \beta_1) + 12 \times (T_2 \cos \beta_2 + N_2^b \sin \beta_2). \quad (\text{B.5})$$

According to equation appendix B.5, the relationship between the elastic modulus of single strand  $E_0$  and the elastic modulus of monofilament  $E$  is as follows, where  $e_8$  is a constant.

$$E_0 = e_8E. \quad (\text{B.6})$$

## Data Availability

The data used to support the findings of this study are available from the corresponding author upon request.

## Conflicts of Interest

The authors declare that there are no conflicts of interest regarding the publication of this paper.

## Acknowledgments

This paper was supported by “Research on Key Technologies of Light and Simple Intelligent Monorail Transporters in Mountainous Orchards”–Key Research and Development Project of Jiangxi Province (Project no. 20171BBF60022) and “Intelligent Management Technology and Equipment for Southern Mountainous Orchards”–2011 Special Fund for Cooperative Innovation in Jiangxi Province (no. 156, GCJZ [2014]). The authors are grateful for the support.

## References

- [1] Y. P. Ouyang, T. S. Hong, J. Su, N. Xu, X. B. Ni, and C. W. Yang, “Design and experiment for rope brake device of mountain orchard traction double-track transporter,” *Transactions of the Chinese Society of Agricultural Engineering*, vol. 30, no. 18, pp. 22–29, 2014.
- [2] M. Kanamitsu, “Multipurpose monorail for hillside orchard,” *Journal of the Japanese Society of Agricultural Machinery*, vol. 70, no. 3, pp. 115–123, 2004.
- [3] O. Koichiro, M. Masahiro, N. Yuji, and I. Nobuhiro, “Automation of farm work by an overhead monorail system in steep sloped citrus orchards,” *Journal of the Japanese Society of Agricultural Machinery*, vol. 58, no. 3, pp. 103–109, 1996.
- [4] Z. Li, P. Xu, Y. P. Ouyang, S. L. Lv, and Q. F. Dai, “Control system for the mountainous orchard electric-drive monorail transporter,” *Applied Mechanics and Materials*, vol. 738–739, pp. 935–940, 2015.
- [5] K. Mikio, S. Yamamoto, A. Keiji, K. Kotaro, and N. Tsukasa, “Development of multipurpose monorail for hillside orchards (Part 2) development of S-shaped monorail system and the results of field test,” *Journal of the Japanese Society of Agricultural Machinery*, vol. 70, no. 3, pp. 115–123, 2008.
- [6] J. Xina, S. Li, and Y. Zhang, “Main parameters calculation and performance test of 7YGS-45 type self-propelled dual-track orchard transport,” in *Proceedings of the International Symposium on Polymer Composites and Polymer Testing*, pp. 232–237, Hangzhou, China, May 2012.
- [7] X. Y. Wang, X. B. Meng, J. X. Wang, Y. H. Sun, and K. Gao, “Mathematical modeling and geometric analysis for wire rope strands,” *Applied Mathematical Modelling*, vol. 39, no. 3–4, pp. 1019–1032, 2015.
- [8] J. F. Beltrán and E. De Vico, “Assessment of static rope behavior with asymmetric damage distribution,” *Engineering Structures*, vol. 86, pp. 84–98, 2015.
- [9] V. Périer, L. Dieng, L. Gaillet, and S. Fouvry, “Influence of an aqueous environment on the fretting behaviour of steel wires used in civil engineering cables,” *Wear*, vol. 271, no. 9, pp. 1585–1593, 2011.
- [10] D. Bruski, “Determination of the bending properties of wire rope used in cable barrier systems,” *Materials*, vol. 13, no. 17, p. 3842, 2020.
- [11] R. H. Knapp, “Derivation of a new stiffness matrix for helically armoured cables considering tension and torsion,” *International Journal for Numerical Methods in Engineering*, vol. 14, no. 4, pp. 515–529, 1979.
- [12] G. A. Costello, “Stresses in multilayered cables,” *Journal of Energy Resources Technology*, vol. 105, no. 3, pp. 337–340, 1983.
- [13] G. A. Costello, *Static Response of a Wire Rope*, pp. 44–57, Springer, New York, NY, USA, 1970.
- [14] G. A. Costello and R. A. Miller, “Lay effect of wire rope,” *Journal of the Engineering Mechanics Division*, vol. 105, no. 4, pp. 597–608, 1979.
- [15] G. A. Costello and J. W. Phillips, “Effective modulus of twisted wire cables,” *Journal of the Engineering Mechanics Division*, vol. 102, no. 1, pp. 171–181, 1976.
- [16] J. W. Phillips and G. A. Costello, “Analysis of wire ropes with internal-wire-rope cores,” *Journal of Applied Mechanics*, vol. 52, no. 3, pp. 510–516, 1985.
- [17] S. A. Velinsky, “Analysis of wire ropes with complex cross-sections,” *Architectural Institute of Japan*, vol. 42, p. 95, 1982.
- [18] S. A. Velinsky, G. L. Anderson, and G. A. Costello, “Wire rope with complex cross sections,” *Journal of Engineering Mechanics*, vol. 110, no. 3, pp. 380–391, 1984.
- [19] L. Liu, S. Zheng, and D. Liu, “Effect of lay direction on the mechanical behavior of multi-strand wire ropes,” *International Journal of Solids and Structures*, vol. 185–186, pp. 89–103, 2020.

- [20] W. Wu and X. Cao, "Mechanics model and its equation of wire rope based on elastic thin rod theory," *International Journal of Solids and Structures*, vol. 102-103, pp. 21-29, 2016.
- [21] H. Pu, X. Xie, S. Jia, and G. Liang, "Research on detection for broken wires in non-rotating rope base on SVM," in *Proceedings of the 2010 International Conference on Electrical and Control Engineering*, pp. 1664-1667, Wuhan, China, June 2010.
- [22] M. Raouf and I. Kraincanic, "Analysis of large diameter steel ropes," *Journal of Engineering Mechanics*, vol. 121, no. 6, pp. 667-675, 1995.
- [23] S. Xue, R. Shen, M. Shao, W. Chen, and R. Miao, "Fatigue failure analysis of steel wire rope sling based on share-splitting slip theory," *Engineering Failure Analysis*, vol. 105, pp. 1189-1200, 2019.
- [24] A. Wahid, N. Mouhib, A. Ouardi, F. Sabah, H. Chakir, and M. Elghorba, "Experimental prediction of wire rope damage by energy method," *Engineering Structures*, vol. 201, Article ID 109794, 2019.
- [25] D. Wang, J. Zhang, S. Ge, D. Zhang, and G. Shi, "Mechanical behavior of hoisting rope in 2km ultra deep coal mine," *Engineering Failure Analysis*, vol. 106, Article ID 104185, 2019.
- [26] Y. P. Ouyang, Q. L. Wu, F. Jiang et al., "Study of design and test analysis of rope breaking brake device for traction orchard conveyer based on eco-mechanical processing Technology," *Ekoloji*, vol. 28, no. 107, pp. 4099-4109, 2019.
- [27] Y. P. Ouyang, H. Su, T. S. Hong, S. R. Su, D. B. Chen, and Z. Q. Wu, "Design and test of wire rope damage test platform for orchard transporter," *Transactions of the Chinese Society for Agricultural Machinery*, vol. 51, no. 7, pp. 118-128, 2020.
- [28] Y. P. Ouyang, T. Y. Wang, H. Su et al., "Spatial structure analysis and geometric modeling of traction wire rope of mountain track carrier," *Journal of Harbin Institute of Technology*, vol. 53, no. 1, pp. 184-192, 2021.
- [29] T. A. Conway and G. A. Costello, "Response of a strand with elliptical outer wires," *International Journal of Solids and Structures*, vol. 28, no. 1, pp. 33-42, 1991.
- [30] T. A. Conway and G. A. Costello, "Viscoelastic response of a simple strand," *International Journal of Solids and Structures*, vol. 30, no. 4, pp. 553-567, 1993.
- [31] R. H. Knapp, "Helical wire stresses in bent cables," *Journal of Offshore Mechanics and Arctic Engineering*, vol. 110, no. 1, p. 55, 1988.
- [32] Y. Wang, "Failure and life prediction of hoisting wire rope," *Mining & Processing Equipment*, vol. 1, no. 10, pp. 13-15, 1991.